Controlling Defects to Achieve Reproducibly High Ionic Conductivity in Na_3SbS_4 Solid Electrolyte

Masaki Shimoda,[a] Mayu Maegawa,[a] Suguru Yoshida,[a] Hirofumi Akamatsu,[a]

Katsuro Hayashi,[a] Prashun Gorai,[b*] Saneyuki Ohno[a*]

[a] *Department of Applied Chemistry, Graduate School of Engineering, Kyushu University, 744*

Motooka, Nishi-ku, 819-0395 Fukuoka, Japan

[b] *Colorado School of Mines, Golden, CO 80401, USA*

E-mail: pgorai@mines.edu, saneyuki.ohno@cstf.kyushu-u.ac.jp

Abstract

The ability to reproducibly synthesize highly conductive solid electrolytes (SEs) is a prerequisite for the widespread usage of solid-state batteries. However, reported ionic conductivities of SEs exhibit significant variation even in materials with same nominal composition. In this study, the thermodynamic origin of such sample-dependent variations are discussed using sodium-ion conducting Na_3SbS_4 as a model SE. The impact of uncontrolled variations in elemental chemical potentials on the ionic conductivity is investigated with theory and experiments. The elemental chemical potentials are uniquely defined when the system is constrained to have zero thermodynamic degrees of freedom. First, we establish the relationship between the chemical potentials and sodium-ion conductivity in Na_3SbS_4 by computing the phase diagram and native defect formation energies. From these calculations, we identify two distinct three-phase equilibrium regions (zero degrees of freedom) with the highest ratio of sodium-ion conductivity, which are then experimentally probed. Transport measurements reveal an abrupt change in the bulk ion transport of the phase-pure samples, with room-temperature ionic conductivity of 0.16 – 1.2 mS cm^{-1} with a standard deviation of 50% when the elemental chemical potentials are not controlled i.e., uniquely defined. In contrast, we show that by controlling the chemical potentials and therefore, the defect formation energies through the experimental concept of *phase boundary mapping*, the sample-dependent variation is reduced to 15% with a high average ionic conductivity of 0.94 mS cm^{-1}. This study highlights the existence of "hidden" thermodynamic states defined by their chemical potentials and the need to precisely control these states to achieve reproducibly high ionic conductivity.

1. Introduction

Solid-state batteries, enabled by inorganic solid electrolytes, are considered safer and more energy-dense alternatives to conventional lithium-ion batteries, operating with organic liquid electrolytes.[1] The key component of solid-state batteries is the solid electrolyte, which needs to possess high ionic conductivity and enable stable interface formation with other components.[2,3] Chemically and electrochemically stable lithium-ion conducting oxides (e.g., lithium garnets,[4–6] Li-NASICONs,[7,8] and perovskites[9]) often form a stable interface with the active materials. More polarizable, ion-conducting sulfides (e.g., Li-argyrodites,[10–13] thio-LISICONs,[14–16], and LGPS family[17–20]) tend to exhibit faster ion transport despite their limited electrochemical stability window.[21,22] New classes of materials, e.g., halides and complex borates,[23–26] have also emerged as promising solid electrolytes, and the list of candidate materials continues to grow. The same is true for sodium-ion (Na-ion) conducting solids,[27–30] which are superior in terms of resource ubiquity and abundance.[31,32]

Recently, among various lithium- and Na-ion conducting solids, Na_3SbS_4 and related compounds have attracted considerable attention due to their high ionic conductivity.[30,33] Na_3SbS_4 crystallizes in cubic $I\bar{4}3m$ or tetragonal $P\bar{4}2_1c$ space groups.[34,35] Whereas mechanochemical synthesis results in the formation of the cubic phase, a solid-state synthesis leads to the tetragonal polymorph (Figure 1a) at room temperature, possessing two Na^+ positions (Wyckoff positions of $4d$ and $2a$) and Sb^{5+} sitting on $2b$ site form SbS_4^{3-} tetrahedra with S^{2-} atoms (Wyckoff $8e$). A recent study, where Sb^{5+} was substituted with W^{6+}, reported a drastic enhancement in the ionic conductivity, which exceeds 30 mS cm^{-1}.[30,33] Subsequent studies involving substitution of Sb^{5+} with Mo^{6+} and S^{2-} with Cl^{1-} further corroborated that decreased Na site occupancy in the structure facilitates faster Na-ion transport in Na_3SbS_4.[36–38] Along with the fact that ionic conductivity rapidly decreases with substitution of tetrels (Si^{4+}, Ge^{4+}, Sn^{4+}) on Sb^{5+} site,[36] it is clearly evident that Na-ion transport in Na_3SbS_4 is mediated by sodium vacancy (V_{Na}) and therefore, it is vital to precisely control V_{Na} concentration to achieve high and reproducible ionic conductivity (Figure 1b).

Despite reports of high ionic conductivity, there are still outstanding challenges for widespread

usage of these solid electrolytes. Reproducibility of ionic conductivity in solid electrolytes is one of those challenges. A large variation in the measured ionic conductivity has been observed even in nominally the same materials. While different synthesis routes often lead to significantly different ionic conductivities,[39] a spread in the measured values may be observed even in the samples prepared via identical synthetic routes. For instance, the reported ionic conductivities of Na_3SbS_4 synthesized by solid-state reaction at 550°C vary from 1.1 mS cm^{-1} to 0.01 mS cm^{-1} despite having the same nominal composition.[30,40,41] An inter-laboratory reproducibility of ionic conductivity measurements has also been evaluated through a round-robin test by distributing identical solid electrolytes homogeneously prepared at one place.[42] Seven different research groups around the world performed impedance spectroscopy with lab-standard procedures on identical samples, revealing a wide spread in the measured ionic conductivity and activation energy. Subsequently, another study showcased that both the stack pressure during the measurement and the fabrication pressure of the sample pellets, can further add to the variability in the measured total ionic conductivity.[43] However, the origin of the sample-dependent variations in ion transport measurements remains unclear. Furthermore, intrinsic variability in the ionic conductivity of solid electrolytes has not been systematically investigated yet. This is partly due to the requirement of a series of experiments performed under identical synthesis and measurement conditions.

Inspired by the high ionic conductivity of Na_3SbS_4, which exhibits large variability, we have investigated a thermodynamic origin of the sample-dependent variation in ionic conductivity by precisely controlling the native defect concentration. From thermodynamics, we know that the elemental chemical potentials of the constituent elements of a material are uniquely defined when the system is constrained to have zero thermodynamic degrees of freedom. Due to the relation between elemental chemical potentials and defect formation energies, shifts in elemental chemical potentials can change the concentration of native defects. Thus, when particular defects mediate the ion transport, a shift in the chemical potential of the conducting ion element will impact the ionic conductivity by altering the native defect concentration. We first elaborated the relationships between elemental chemical potentials, phase equilibria, formation energies of native defects, and ion transport, based on the calculated Na-Sb-

S ternary phase diagram and the formation energies of the native defects in Na_3SbS_4. Following the experimental assessment of the phase diagram at room temperature, we identified the range of nominal compositions where the chemical potential changes abruptly by using the experimental concept of *phase boundary mapping*. By preparing a series of samples that straddle these critical nominal compositions causing a shift in the chemical potentials, it was found that the resulting ionic conductivity values ranged from 0.16 to 1.2 mS cm^{-1} and their relative standard deviation was almost 50%, highlighting the need for controlling the native defects. In contrast, reproducibly high ionic conductivity with significantly lower deviation (~16%) was achieved by controlling the thermodynamic states. In addition, the change in the bulk ionic conductivity arising from variation in native defects was found to be more significant than that in macroscopic ion transport due to the formation of the competing phases. This study sheds light on the importance of controlling the hidden parameters, *i.e.*, the *thermodynamic states*, defined by elemental chemical potentials in achieving reproducible ionic conductivity. Despite its thermodynamic grounding, this "hidden" knob has been somewhat overlooked; controlling this knob has practical implications for the mass production of solid electrolytes with high performance for practical use.
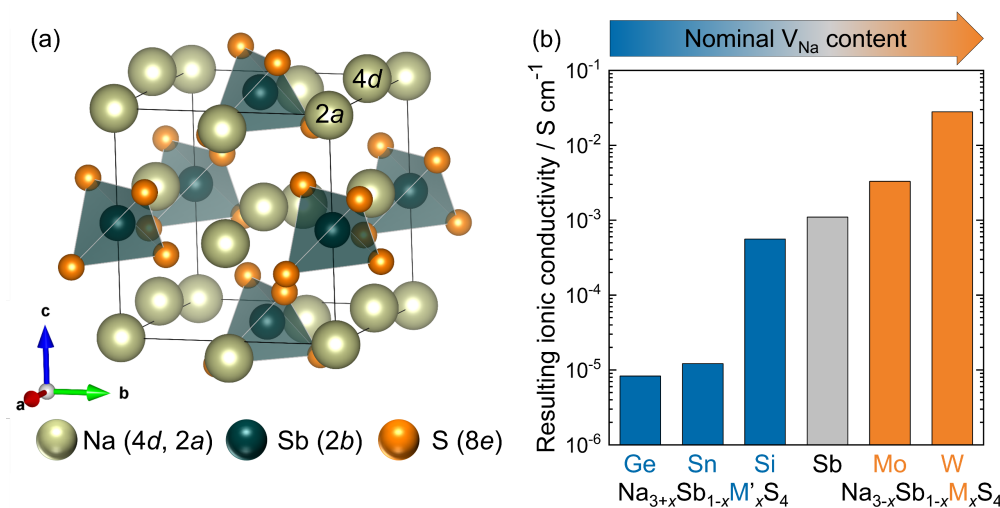

***Figure 1**: (a) Structure of tetragonal Na_3SbS_4 (space group of $P\bar{4}2_1c$). (b) Na vacancy-mediated transport in Na_3SbS_4 has been experimentally demonstrated by aliovalent substitution. Increasing Na (decreasing Na vacancy concentration) by doping with tetrels M'^{4+} (Si, Ge, Sn) decreases the ionic conductivity. In contrast, introducing additional Na vacancies by substituting Sb^{5+} with M^{6+} (Mo, W) enhances ionic conductivity. The data is taken from Refs. 30,33,36,44.*

2. Methods

Synthesis. Samples containing Na_3SbS_4 were synthesized via solid-state reaction in a sealed quartz ampule using Na_2S (98%, Sigma-Aldrich), Sb (99.5%, FUJIFILM Wako Pure Chemical Corporation), S (reagent grade, Sigma-Aldrich), and Sb_2S_3 as procurers. Sb_2S_3 was synthesized in-house with stoichiometric amounts of Sb and S, sealed in a quartz ampule. The sealed ampule was heated to 650 °C at 100 °C h^{-1} and kept for 20 minutes. The temperature was then lowered to 500 °C at a rate of 20 °C h^{-1} and kept for 24 hours before turning off the furnace. The obtained Sb_2S_3 was ground to a powder in an agate mortar for about 15 minutes before usage. Samples with nominal compositions of $Na_{3.13}SbS_{4+x}$ ($x = 0.01, 0.05, 0.06, 0.07, 0.08, 0.09, 0.1, 0.14, 0.15, 0.23$, and 0.28) were synthesized with Na_2S, S, and Sb_2S_3. The excess Na was necessary to reduce side phase fractions, indicating some losses of Na during synthesis. Stoichiometric amounts of precursors were dry-mixed in an agate mortar for 15 minutes. The homogenized mixture was pelletized with a uniaxial press at around 300 MPa. The resulting pellets were vacuum-sealed in a carbon-coated quartz ampoule. The prepared carbon-coated quartz ampules were annealed under a vacuum at 800 °C for 1.5 hours to remove any trace of moisture before loading samples. The sealed ampules were heated to 550 °C at a rate of 30 °C h^{-1} and kept for 20 hours to complete the reaction. The temperature was then lowered to 200 °C at a rate of 30 °C h^{-1} and kept for 24 hours to anneal the solid phases before cooling them to room temperature. The resulting pellets were hand ground to a powder in an agate mortar for 15 minutes before characterization. Besides, samples with nominal compositions of $Na_{1.22}SbS_{2.11}$ were synthesized to obtain a diffraction pattern of a new polymorph of $NaSbS_2$ and to confirm that there is another three-phase equilibrium.

Synchrotron powder X-ray diffraction. Phase identification was carried out using the beamline BL02B2 at SPring-8 in Japan. The large Debye-Scherrer camera with six MYTHEN solid-state detectors constitute the diffractometer. The powder samples were housed in a Lindemann capillary tube with an inner diameter 0.2 mm. The wavelength used for the measurement was determined to be 0.7745 Å by performing wavelength calibration using CeO_2 as a standard sample. The measurement results were

analyzed by Pawley fitting using TOPAS-Academic V6 software[45] to identify the side phases and their fractions. A pseudo-Voigt function using the modified Thomson–Cox–Hastings setting was utilized for the peak shape. A scale factor, Chebyshev background with 20 coefficients, lattice parameters, zero-point shift, and peak shape were refined for the fitting. Crystal structures were visualized by VESTA software package.[46]

Temperature-dependent impedance spectroscopy. The total ionic conductivities and activation energies of the obtained samples were measured by temperature-dependent impedance spectroscopy. Impedance measurement was performed by packing the sample powder in a house-made press cell to maintain the external pressure during the measurement. Aluminum foils were placed as a current collector between the sample powder and the stainless rods. All cells were constructed in a glove box, and the samples inside the press cell were O-ring sealed to avoid air exposure. The cell pressure of about 60 MPa was applied with a torque screw attached to the external duralumin frame. The constructed cells were connected to a VMP3 impedance analyzer (manufactured by Biologics) and placed in the temperature-controlled furnace (manufactured by Espec). A voltage amplitude was 20 mV, and a frequency range was from 1MHz to 100 mHz. The temperature was varied from −40 to 60 °C with 10 °C steps, as well as 25 °C. The measured spectra were fitted by equivalent circuits using Relaxis3 (rhd instruments).

Native defect energetics, electronic structure, and phase diagram: The formation energy of native defects in tetragonal Na_3SbS_4 was calculated with density functional theory (DFT) using the standard supercell approach.[47] Within the supercell approach, the formation energy of a defect D in charge state q ($\Delta E_{D,q}$) is given by,

$$\Delta E_{D,q} = \left(E_{D,q} - E_H\right) + \sum_i n_i \mu_i + q E_F + E_{\text{corr}} \tag{1}$$

where E_H and $E_{D,q}$ are the total energy of the defect-free, charge neutral host supercell and the supercell containing defect D in charge q, respectively. The elemental chemical potential of element i is denoted by μ_i and n_i is the number of atoms of element i removed ($n_i > 0$) or added ($n_i < 0$) from the supercell

6

to create the defect D. E_F is the Fermi energy, which is typically referenced to the valence band maximum (VBM) i.e., $E_F = 0$ eV at the VBM. The approach to calculating $\Delta E_{D,q}$ suffers from artifacts arising due to the use of finite-sized periodic supercells.[47] Additional artifacts are often introduced due to DFT limitations, most notably, the underestimation of the band gap with standard exchange-correlation functionals. Various *ad hoc* schemes are available to correct for the finite-size artefacts and inaccurate electronic structure; these corrections are represented by the term E_{corr} in Eq (1).

The total energies of the supercells were calculated using the GGA-PBE functional within the projector augmented wave (PAW) formalism[48] as implemented in the Vienna Ab Initio Simulation Package.[49] Plane waves were expanded with energy cutoff of 340 eV and a Γ-centered 4×4×4 Monkhorst-Pack k-point grid was used to sample the Brillouin zone. The position of the ions in the defect supercells were relaxed following the procedures similar to that adopted in Ref. 50. Supercells containing 128 atoms were used in the defect calculations. The chemical potential of element i, μ_i, is expressed relative to its reference phase under standard conditions (μ_i^0) as $\mu_i = \mu_i^0 + \Delta\mu_i$. $\Delta\mu_i$ is the deviation from the reference and $\Delta\mu_i \leq 0$. The maximum, $\Delta\mu_i = 0$, corresponds to the element i-rich condition. The reference chemical potentials μ_i^0 were fitted to a set of measured formation enthalpies. The fitted μ_i^0 values are listed in Table S3 of the supplementary information. The range of values of $\Delta\mu_{Na}$, $\Delta\mu_{Sb}$, and $\Delta\mu_S$ are bound by the condition of phase stability of Na_3SbS_4 and the additional constraints imposed by the instability of the competing phases in the ternary Na-Sb-S chemical space. In total, we considered 11 competing phases reported in the ICSD (Table S4).

The underestimation of the band gap in DFT (PBE-GGA) is corrected by applying band edge shifts calculated using the GW approximation.[51] Specifically, the starting DFT wave functions were fixed, while the GW eigenvalues were iterated till self-consistency. Fixing the DFT wave functions allows the interpretation of the GW quasiparticles energies in terms of energy shift relative to Kohn-Sham energies. The GW calculations were performed using a Γ-centered 8×8×8 k-point grid. Lastly, E_{corr} in Eq. (1) contains corrections for: (i) artificial electrostatic interactions between periodic images of defect point charges, (ii) misalignment of the average electrostatic potentials between supercells with and without

charged defects, (iii) Moss-Burstein type band filling due to shallow defects, and (iv) band edge shifts

for shallow acceptors/donors. The defect calculations were set up and analyzed using the pylada-defect

software.[52]

3.   Results and Discussion

3.1 Thermodynamic states of Na_3SbS_4 and their relation to ion transport

According to the Gibbs phase rule, the degrees of freedom (F) in a ternary system ($C = 3$) at constant

pressure and temperature in three-phase equilibrium ($P = 3$) is zero because $F = C - P$. Put differently,

the elemental chemical potentials in the ternary system are uniquely defined in the three-phase

equilibrium region. Therefore, the compositions of the phases that are in the three-phase equilibrium

remain unchanged, and only their phase fractions can vary. Conversely, when a ternary compound of

interest is synthesized in equilibrium with two different sets of equilibrium phases (two side phases),

then the elemental chemical potentials in one sample must differ from the other. Due to the

thermodynamic origin of this difference, we can say that the two samples are in different *thermodynamic*

states.[53]

Let us consider the case of the tetragonal Na_3SbS_4. Figure 2(a) shows the computed Na-Sb-S

ternary composition phase diagram based on the formation enthalpies determined from DFT total

energies and fitted reference chemical potentials (see Methods, Table S3). Figure 2(b) shows a zoomed-

in version of the phase diagram in the vicinity of Na_3SbS_4. We predict that Na_3SbS_4 shares tie lines with

five other equilibrium phases (Na_3SbS_3, $NaSbS_2$, Na_2S, NaS and NaS_2); consequently, Na_3SbS_4 is

surrounded by five distinct three-phase equilibria (regions 1 – 5 in Figure 2b). As discussed above, the

elemental chemical potentials of Na_3SbS_4 in each of the three-phase regions are fixed and remain

unchanged even if the sample composition varies as long as it resides in the same three-phase

equilibrium. Therefore, in theory, Na_3SbS_4 equilibrated at fixed pressure and temperature possesses five

different *thermodynamic states*. Importantly, Na_3SbS_4 in different *thermodynamic states* is expected to

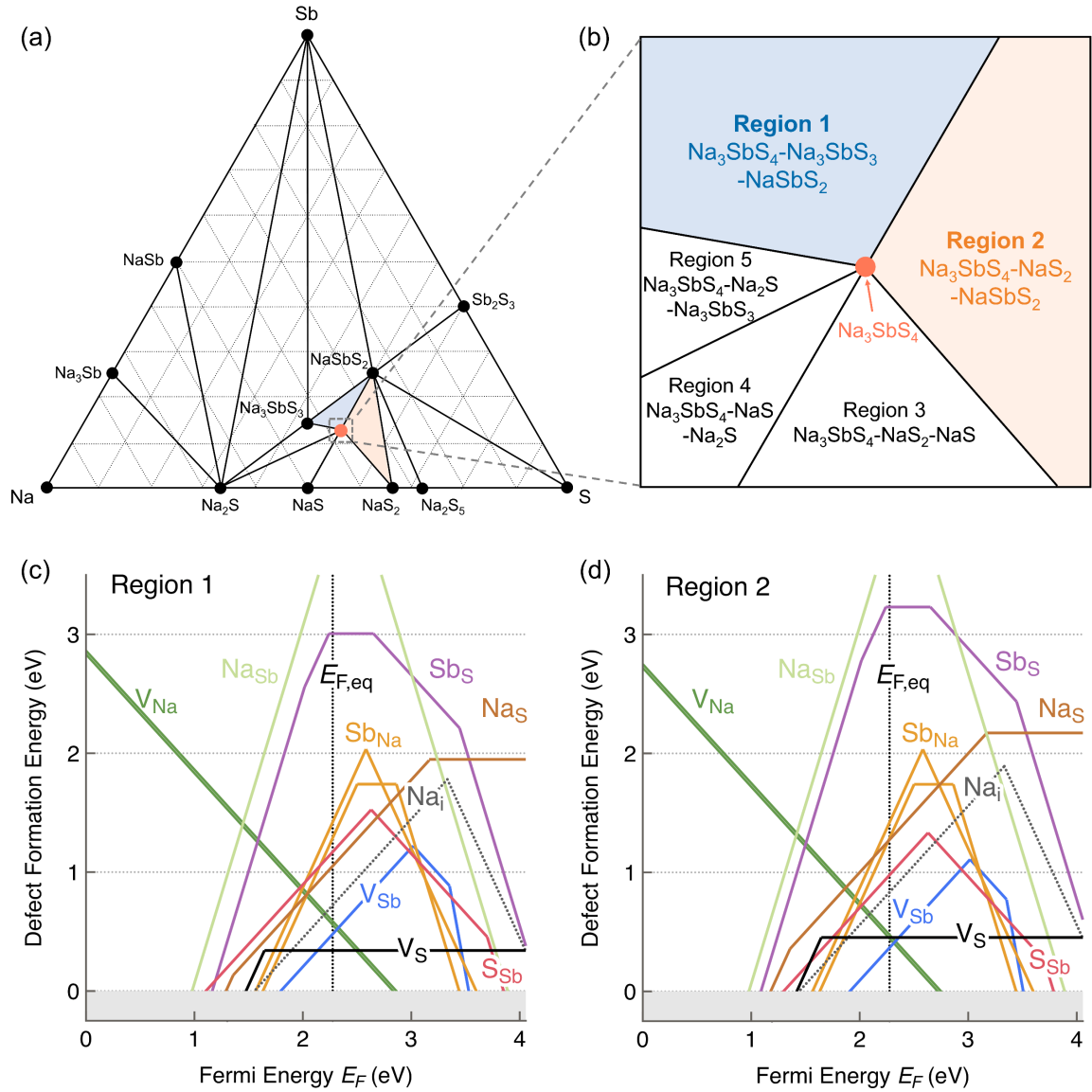exhibit different ion transport properties, especially when the transport is mediated by a particular defect.

8

Figure 2*: (a) Theoretically predicted Na-Sb-S ternary phase diagram shows that there are five distinct three-phase equilibria around Na₃SbS₄ phase, which are enlarged in (b). All the competing phases that coexist in equilibrium with Na₃SbS₄ are in the solid state at the typical sintering temperature of 200°C. (c, d) Formation energy ($\Delta E_{D,q}$) of native defects as a function of the Fermi energy (E_F) in the three-phase equilibrium regions 1 and 2. E_F is referenced to the valence band maximum. The upper limit of E_F shown is the conduction band minimum such that E_F ranges from 0.0 eV to the band gap (4.1 eV). Formation energy of different defect types are plotted in different colors. Multiple lines of the same color represent defects at unique Wyckoff sites e.g., V_{Na} two Na Wyckoff sites. The equilibrium $E_{F,eq}$ is calculated at the synthesis temperature of 823 K and marked by vertical dotted lines. At the equilibrium (E_F), the dominant defects are V_{Na}^{-1}, V_S^0, and V_{Sb}^{+1}. The V_{Na}^{-1} concentration in region 2 is half an order of magnitude higher than in region 1 (Table S2).*

Figures 2(c) and 2(d) show the calculated formation energies ($\Delta E_{D,q}$) of native defects (vacancies, interstitials, and anti-site defects) in Na_3SbS_4 as a function of the Fermi energy (E_F) in regions 1 and 2, respectively. The slopes of the defect lines in Figure 2(c, d) represent the charge states and conventionally, only the lowest-energy charge state at a given E_F is shown. Based on charge neutrality, the equilibrium Fermi energy ($E_{F,eq}$) lies in the vicinity of the intersection of acceptor sodium vacancy (V_{Na}) and donor antimony vacancy (V_{Sb}). V_{Na} has formation energy around 0.56 eV and 0.44 eV at $E_{F,eq}$ in regions 1 and 2, respectively, suggesting that V_{Na} is natively present in high concentrations ($>10^{19}$ cm^{-3}, Table S2) in undoped Na_3SbS_4. V_{Na} also has significantly lower formation energy than Na interstitials (Na_i). At the synthesis temperature of 823 K, the concentration of V_{Na} is three orders of magnitude higher than that of Na_i (Table S2), supporting that Na diffusion mechanism in Na_3SbS_4 is known to be mediated by Na vacancies.[30,33] Furthermore, Figures 2(c, d) show that V_{Sb} and V_S have comparable formation energies to V_{Na}, indicating that they are also present in high concentrations in Na_3SbS_4. In particular, V_S^0 is present in concentrations in excess of 10^{19}-10^{20} cm^{-3}. The equilibrium Fermi energy calculated at 823 K (assuming "frozen" defects) determines the net carrier concentration ([n-h]). We find that [n-h] is around 10^9-10^{10} cm^{-3} (Table S2). Given their low formation energies, V_S and V_{Sb} are the dominant donor defects. However, at $E_{F,eq}$, V_S exists in a neutral charge state, and therefore, does not generate charge carriers. In addition, electrons donated by V_{Sb} are trapped by its own deep level states located at E_F ~3.0 and ~3.4 eV. In other words, the net electrons are not free carriers; the electrons will be trapped at these deep defect states and unlikely to be activated/ionized even at higher temperatures because the defects states are significantly deep. As a result, very low electronic conductivity is expected in Na_3SbS_4.

Na_3SbS_4 in the three-phase regions 1 and 2 are in different thermodynamic states and chemical potentials of constituent elements ($\mu_i = \mu_i^0 + \Delta\mu_i$, where i = Na, Sb, or S) are uniquely determined by the formation energies of the co-existing equilibrium phases. The values are tabulated in Table S1. Comparing $\Delta\mu_{Na}$ in regions 1 and 2, $\Delta\mu_{Na}$ in region 2 ($\Delta\mu_{Na} = -1.971$ eV) is lower than that in region 1 (($\Delta\mu_{Na} = -1.859$ eV), $i.e.$ the region 2 is more Na-deficient (μ_{Na} in region 2 < μ_{Na} in region 1). Thus, with the following relation between the Na chemical potential and V_{Na} formation energy can

be written (specific case of Eq. 1),

$$\Delta E_{V_{Na}} = \left(E_{V_{Na}} - E_H\right) + \mu_{Na} - E_F + E_{corr}, \qquad (2)$$

we can conclude that V_{Na} formation energy is lower and V_{Na} concentration is higher in region 2. Given that Na-ion conduction in Na_3SbS_4 is mediated by V_{Na}, the Na ion conductivity (σ_{ion}) of Na_3SbS_4 phase is expected to be higher in the thermodynamic state defined by region 2. Interestingly, we find that due to the overall charge balance, the highest ratio of V_{Na} concentration is between regions 2 and 1, among the 5 different thermodynamic states shown in Table S1. Overall, controlling the *thermodynamic state* of the sample can tune the native defect concentration and, with it, ionic transport. In the case of Na_3SbS_4, the sample in region 2 is predicted to possess the highest ionic conductivity because it represents the most Na-poor thermodynamic condition ($\Delta\mu_{Na}$ most negative in Table S1) with highest V_{Na} concentration.

There is only a small difference in the chemical potential of Na among the 5 thermodynamic states (Table S1), which is attributed to the small stability window of tetragonal Na_3SbS_4. Nonetheless, at a synthesis temperature of 823 K, such a small difference in chemical potential can still give rise to half an order of magnitude difference in the concentration of V_{Na} (Table S2).

3.2 Experimental exploration of different thermodynamic states

To experimentally access the different *thermodynamic states* and assess their impact on ion transport, samples containing different sets of co-existing/competing phases were prepared. The nominal compositions of the two samples were $Na_{3.03}SbS_{3.92}$ (Na-rich sample) and $Na_{3.13}SbS_{4.23}$ (Na-deficient sample), respectively, to target regions 1 and 2 (Figure 2b). Slightly excess Na was necessary in the synthesis because the stoichiometric composition (Na_3SbS_4) led to a significant amount of impurity (e.g. $NaSbS_2$ with a space group of *C*2/*c*).

The synchrotron powder diffraction data from the two representative samples revealed an unreported phase forming another three-phase region between region 1 and region 2. The Powley fitting results of the two diffractograms are shown in Figure 3(a) and 3(b). The new phase was found in the

Na-rich sample, and the associated reflections were well fitted by a rhombohedral $LiSbS_2$ structure

crystalizing in $AgAsS_2$-type structure with a space group of $R\overline{3}$, hence this phase is referred to as $NaSbS_2$

($R\overline{3}$) hereafter. Interestingly, a sample with a nominal composition of $Na_{1.22}SbS_{2.11}$ disclosed that there

is another three-phase region, Na_3SbS_4-$NaSbS_2(R\overline{3})$-$NaSbS_2(C2/c)$, in between regions 1 and region 2,

indicating that either or both $NaSbS_2$ phases are likely off-stoichiometric (see also Figure S1). The

experimentally determined new three-phase equilibrium (region 1.5) is highlighted with a gray-color

area in Figure 3(c). Based on the side phases, the Na-rich sample is undoubtedly located in region 1.

Although only $NaSbS_2$ ($C2/c$) was found with the matrix Na_3SbS_4 in the Na-deficient sample, this

Na_3SbS_4 must be in a different and more Na-deficient *thermodynamic state* than in the Na-rich sample.

Temperature-dependent impedance spectroscopy was performed to assess the difference in the

resulting ion transport in Na_3SbS_4 in the two different thermodynamic states. Figure 4(a) and 4(b) show

Nyquist plots of the two samples measured at −40 °C. The data from the Na-rich sample (Figure 4a)

was fit with an equivalent circuit consisting of a parallel constant-phase element (CPE) / resistor (R) in

series with a CPE, representing stainless-steel ion blocking electrodes. Although the deconvolution of

the bulk (R_B) and grain boundary (R_{GB}) processes was not possible within the measured temperature

range, the capacitance of the process calculated via the Brug formula was 6.5 pF and the ideality factor

of the process was 0.8.[54] Considering the impedance measurement performed in the press cell

configuration typically results in slightly deformed semicircle,[42] this semicircle most likely arises from

the ion transport within the bulk.[55] In contrast, the Na-deficient sample (Figure 4b) required a series of

simple resistance and CPE_1/R followed by another CPE_2. The capacitance of the CPE_1 was 180 pF with

the ideality factor of 0.73, indicating that this process is from the grain boundary contribution. Thus the

offset in the Nyquist plot is attributable to the bulk process.[55] Comparing the data from the two samples,

it is evident that the total resistance ($R_{total} = R_B + R_{GB}$) of the Na-rich sample is larger than that of the Na-

deficient sample. This difference cannot be explained by the contribution from the grain boundary

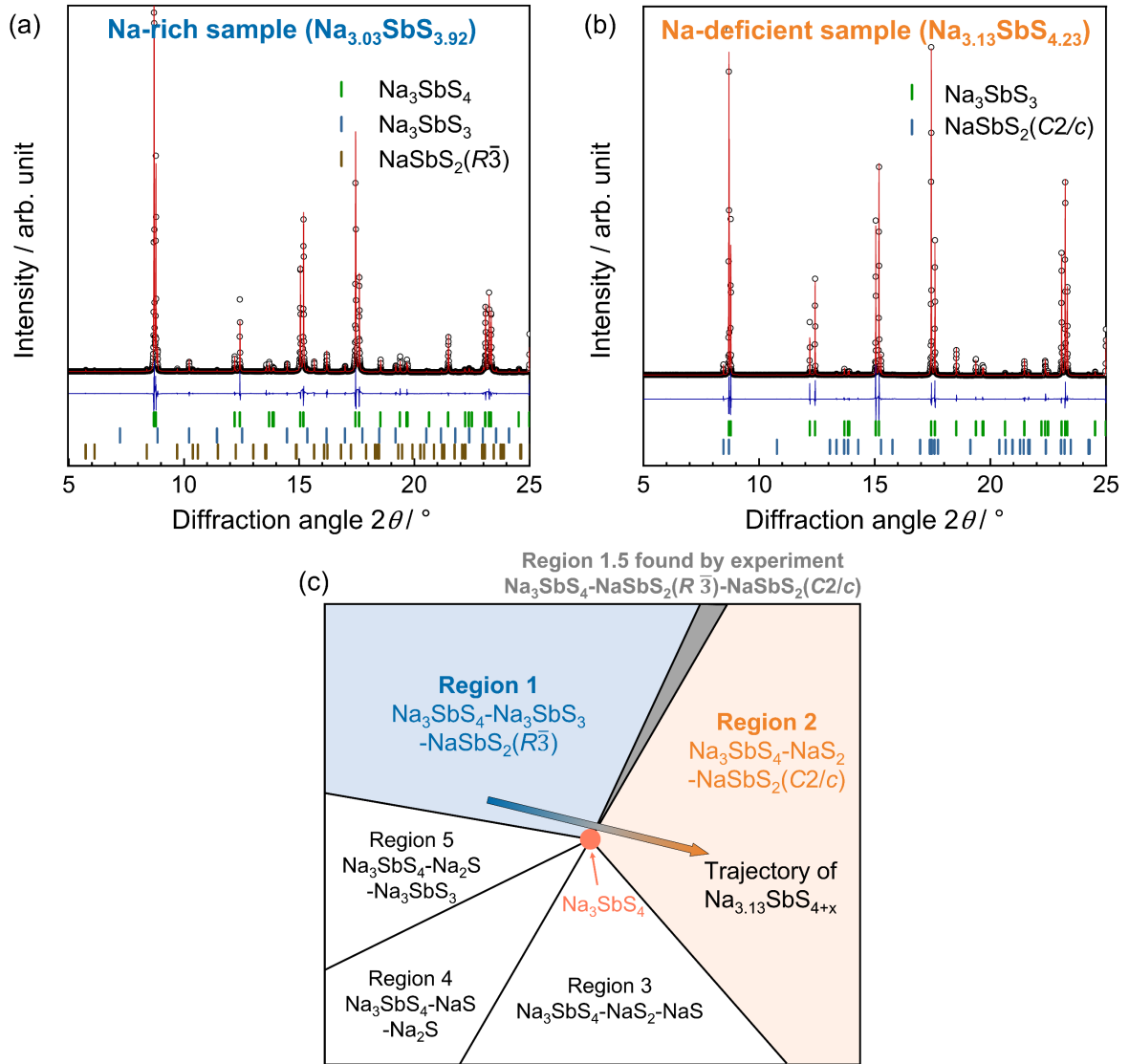because the major difference is from the bulk process.

Figure 3: *(a) and (b) show the synchrotron diffraction data from the samples with nominal compositions of $Na_{3.03}SbS_{3.92}$ (Na-rich sample) and $Na_{3.13}SbS_{4.23}$ (Na-deficient sample), respectively, and their Pawley fits. The confirmed coexisting phases revealed a new $NaSbS_2$ phase crystalizing into the rhombohedral structure with a space group of $R\bar{3}$, which locates in between region 1 and region 2 (the gray-colored region) as shown in (c).*

Figure 4(c) shows the Arrhenius plot of the ionic conductivity obtained from the total resistance measured as a function of temperature. It should be noted that, at higher temperatures, fits were performed with a series circuit of R-CPE. This is because the thermally activated ion transport became too fast to fit with a semicircle reliably. The activation energies, E_a, of the two samples obtained

from the slopes in Figure 4(c), are both 0.26 eV, despite a clear difference in the ionic conductivity. The here-observed change in ion transport can be well explained with the general expression of the ionic conductivity σ,

$$\sigma = \frac{\gamma c \nu e^2 a^2}{k_B T} \exp\left(-\frac{\Delta G_m}{k_B T}\right), \tag{3}$$

where γ is a geometrical factor, c is a concentration of carrier involved in diffusion, ν is an attempt frequency, e is the elementary charge, a is a jump distance, k_B is the Boltzmann constant, and ΔG_m is the free energy of migration.[2] Whereas a subtle difference in the defect formation energy is expected to have a minor impact on the measured activation energies, a discrete and significant difference in the defect concentrations can drastically affect the ionic conductivity.
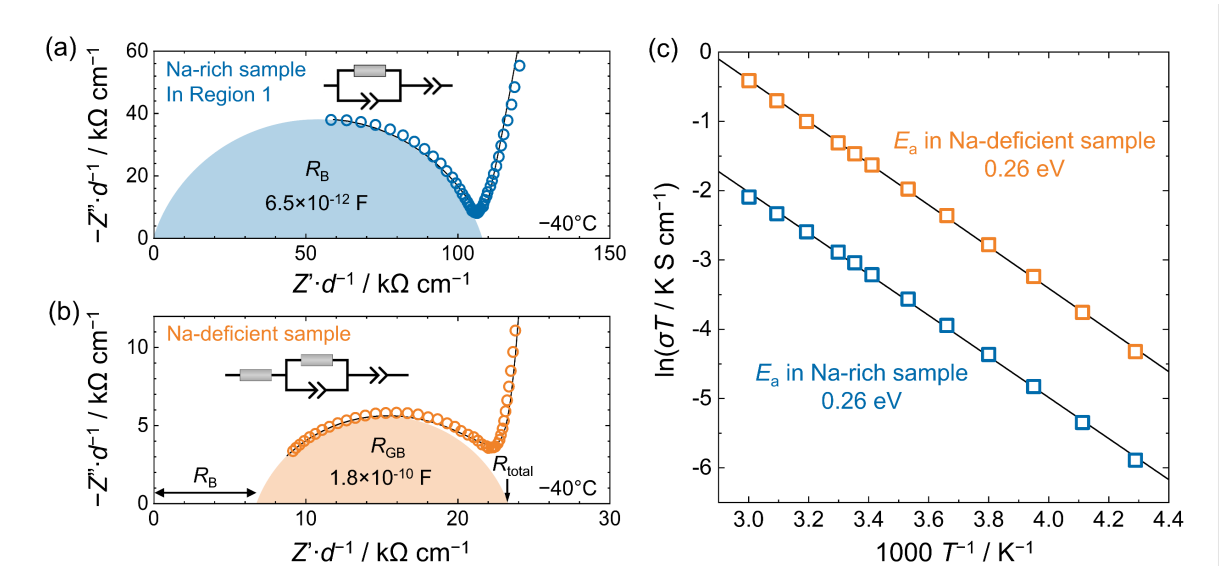

Figure 4: *(a) The Nyquist plot with the data from the Na-rich sample in region 1 shows a semicircle with a capacitance in the order of pF, followed by a blocking tail, indicating the mostly bulk contribution to the total resistance. (b) The Nyquist plot of data from Na-deficient sample likely in region 2 visualizes the total resistance that is significantly lower than that of sample 1 and consists of both bulk and grain boundary contributions. Both data were measured at −40 °C as ion transport become too fast to deconvolute the bulk and grain boundary processes at higher temperatures. For the sake of easier comparison, Z' and Z" are normalized by the thickness of the samples. The electrode area is 0.785 cm². (c) Arrhenius plot of the two samples based on the total resistances, highlighting that there is no significant difference in the activation barriers, despite the evident difference in the ionic conductivity.*

3.3 Phase boundary mapping to precisely access different thermodynamic states

The thermodynamic state remains unchanged within the three-phase equilibrium region, and with it, the microscopic ion transport in a target phase is expected to be unchanged. However, it is empirically known that the grain boundary resistance can greatly vary when the side (impurity) phase fraction changes, drastically altering the macroscopic ionic conductivity. So far, the trends in transport and other parameters at the vicinity of the boundary between the phase regions remain elusive. Therefore, we investigated a series of samples with precisely controlled compositions synthesized and characterized under identical conditions. The nominal sample composition of $Na_{3.13}SbS_{4+x}$ ($0.01 \leq x \leq 0.28$) was selected to go across the boundary of the phase equilibria with only a minute but detectable fractions of side phases. Table 1 summarizes the phases determined by synchrotron XRD. As expected, the matrix phase in all the samples was tetragonal Na_3SbS_4. When $0.09 \leq x \leq 0.17$, Na_3SbS_4 was the only detectable phase, namely, the samples were *phase pure*. When $x < 0.09$, minor peaks of Na_3SbS_3 appeared. $NaSbS_2$ ($C2/c$) appeared when $x > 0.17$. As discussed in section 3.2, Na_3SbS_4 coexisting with Na_3SbS_3 must be in a different thermodynamic state from Na_3SbS_4 coexisting with $NaSbS_2$ ($C2/c$). In other words, despite the detection of the only one side phase at most, the sample composition departed from a Na-rich region must enter the more S-rich region with increasing x in the range of $0.01 \leq x \leq 0.28$. Thus, we denote the thermodynamic state of Na_3SbS_4 with Na_3SbS_3 as Na-rich and the one with $NaSbS_2$ as S-rich (see Table 1).

Table 1. *The nominal sample compositions, phases found in the resulting samples, and the corresponding thermodynamic states of Na_3SbS_4.*

x in $Na_{3.13}SbS_{4+x}$	Existing phases	Thermodynamic state
0.01	Na_3SbS_4, Na_3SbS_3	Na-rich
0.05	Na_3SbS_4, Na_3SbS_3	Na-rich
0.06	Na_3SbS_4, Na_3SbS_3	Na-rich
0.07	Na_3SbS_4	-
0.08	Na_3SbS_4, Na_3SbS_3	Na-rich

0.09	Na_3SbS_4	-
0.10	Na_3SbS_4	-
0.14	Na_3SbS_4	-
0.15	Na_3SbS_4	-
0.23	Na_3SbS_4, $NaSbS_2$ ($C2/c$)	S-rich
0.28	Na_3SbS_4, $NaSbS_2$ ($C2/c$)	S-rich

Figure 5 shows the lattice parameters of the matrix Na_3SbS_4 and room-temperature ionic conductivity of synthesized samples as a function of sulfur content x. Individual impedance results are summarized in Table S5 – S8. The light-gray area in Figure 5(a) ($0.09 \leq x \leq 0.17$) represents the composition range of the *phase-pure* samples where no side phases were observed. There is no systematic change in the lattice parameter despite the change in the thermodynamic state. This is likely due to the narrow compositional range of Na_3SbS_4 as predicted by the theoretical calculations. On the other hand, the room-temperature ionic conductivity showed a stepwise increase by more than twofold from 0.42 mS cm^{-1} to 0.94 mS cm^{-1}. This abrupt change in ion transport clearly indicates the shift in the thermodynamic state within $0.1 < x < 0.14$ (dark-gray area in Figure 5(b)), *i.e.,* the sample composition entered the different phase equilibria within this composition range, causing a discrete change in chemical potentials and the concentration of native defects. The symbol colors in Figure 5(b) is based on the measured ionic conductivity. It is noteworthy that the sudden change occurred in the *phase-pure* composition region. If a sample is prepared to be *phase-pure*, one will not know the precise location w.r.t. the phase boundary until transport measurements are performed. As revealed in the two representative samples in the previous section, the fitting results of impedance spectra measured at −40 °C summarized in Table S7 and S8 highlight that the drastic changes are in the bulk ion transport.
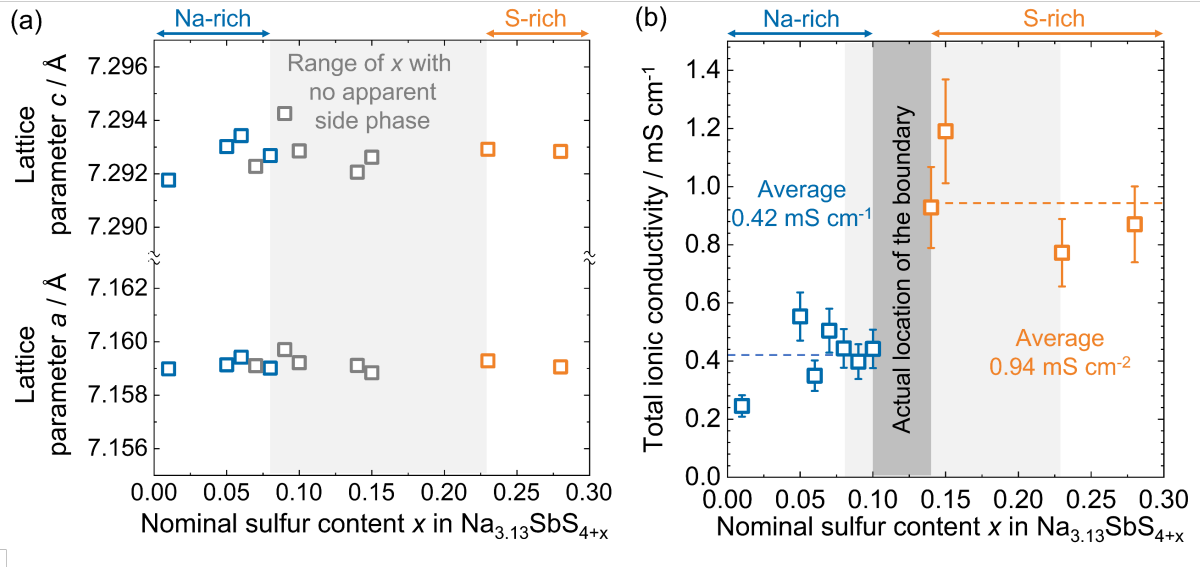
16

Figure 5: *(a) Lattice parameters a and c of the matrix Na_3SbS_4 phase as a function of the sulfur content x in the nominal sample composition of $Na_{3.13}SbS_{4+x}$ remains constant despite the change in the thermodynamic states. Blue and orange symbols represent their thermodynamic states (Na-rich or S-rich) based on the determined side phases. Light-gray color symbols are the data from the phase pure samples. (b) Room-temperature ionic conductivity obtained from the total resistance of all prepared samples shows a stepwise change, highlighting the x value at which there is a shift in the thermodynamic states (the dark-gray range). Colors of the symbols in (b) are based on the observed conductivity and the error bars represent 15 % error.*

In contrast, the spread in the ionic conductivity within the same thermodynamic state is small. Thus, at least at the vicinity of the phase boundary, the change in microscopic ion transport within the matrix phase due to the difference in the thermodynamic state is larger than the change in macroscopic ion transport due to the variation in the amount of a side phase. Figure 6 shows a statistical analysis of the observed conductivity variation in box plots and relative standard deviations. The relative standard deviation of all the samples prepared in this study is about 46% and the conductivity value ranges over an order of magnitude. However, this large spread in conductivity is reduced to 16% within the same thermodynamic state. Therefore, in order to achieve high conductivity with good reproducibility, it is more realistic to define the thermodynamic state by intentionally introducing a small amount of side phase(s) rather than pursuing a phase-pure sample. This way we can precisely specify the

thermodynamic state to make it more favorable for high ionic conductivity. As expected, the activation energies in all the samples remains unchanged (Figure S2), which further corroborates that migration barriers remain almost unchanged in the different thermodynamic states. The changes in ionic conductivity are a direct result of the differences in the V_{Na} concentrations.
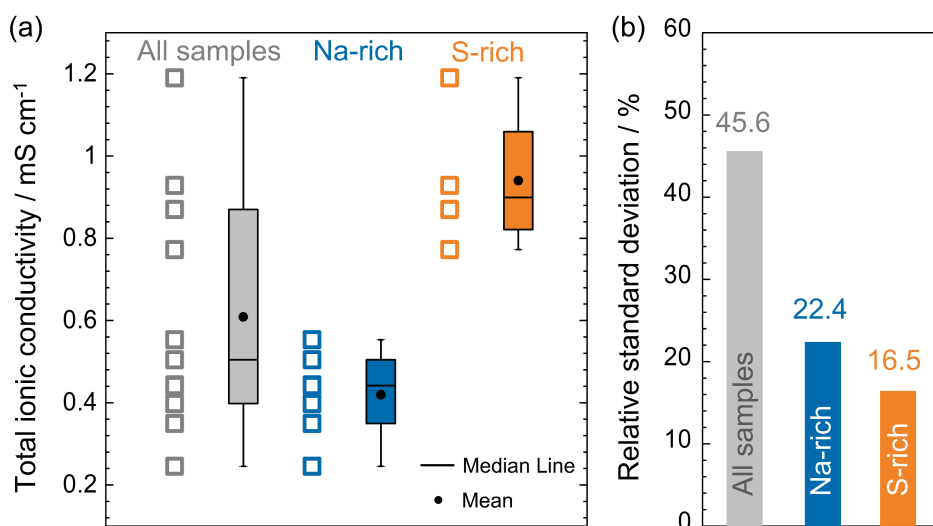

Figure 6*: (a) Box plots for the room-temperature total ionic conductivity of three different groups of samples, all samples, Na-rich samples, and S-rich samples. (b) Relative standard deviation highlights the importance of defining the thermodynamic states toward high reproducibility.*

The experimental concept that enables the full exploration of experimentally-accessible thermodynamic states in polycrystalline bulk samples is called *phase boundary mapping*,[53,56] and it was originally formulated in the field of semiconductors (e.g. thermoelectrics).[57–61] As demonstrated above, through the preparation of a series of samples with systematically controlled nominal compositions, it is possible to map out the locations of the boundaries between phase regions in the nominal-composition space based on the existence of side phases, which enables us to correlate the observed physical properties to their corresponding thermodynamic states. Furthermore, utilization of samples that are constrained with zero degrees of freedom (in thermodynamic equilibrium) can make the resulting properties resilient to compositional variations due to the elemental off-stoichiometry during the preparation.

18

4. Conclusion

We established the theoretical relationships between elemental chemical potentials, defect formation energies, and ion transport using fundamental thermodynamic principles. We identified two equilibrium phase regions (or *thermodynamic states*, as defined by their chemical potentials) that maximize and minimize Na-ion conductivity in Na_3SbS_4. Subsequently, we synthesized Na_3SbS_4 in these two uniquely defined thermodynamic states and demonstrated a noticeable difference in the bulk ionic conductivity, in agreement with our theoretical predictions. We utilized an experimental concept called *phase boundary mapping* to perform a series of carefully controlled experiments in the vicinity of the composition range where a sudden chemical potential change occurs. Transport measurements revealed an abrupt change in the bulk ionic conductivity in this narrow compositional range, while the macroscopic transport is found to be more resilient to compositional variation on either side of this range. From a theoretical perspective, our results highlight the vital role of the thermodynamic states in uniquely defining the chemical potentials, and therefore, the defect concentrations and ionic conductivity. Practically, our findings indicate that the intentional inclusion of a small but detectable amount of side phases is more effective than aiming for a phase-pure sample to synthesize solid electrolytes with reproducibly high ionic conductivity.

■ AUTHOR INFORMATION

Supporting Information

The Supporting information is available free of charge on the ACS Publications website.

Calculated elemental chemical potentials in different phase equilibria; native defect and electronic carrier concentrations; fitted reference elemental chemical potentials; list of the competing phases in the ternary Na-Sb-S chemical space; synchrotron data of the sample with the nominal composition of $Na_{1.22}SbS_{2.11}$; all the fitting results of individual impedance spectra; activation energies of all the samples.

■ AUTHOR INFORMATION
Corresponding Authors
Saneyuki Ohno
Prashun Gorai

Notes

The authors declare no competing financial interest.

■ **REFERENCES**

(1)   Janek, J.; Zeier, W. G. A Solid Future for Battery Development. *Nat. Energy* **2016**, *1* (9), 16141.

(2)   Ohno, S.; Banik, A.; Dewald, G. F.; Kraft, M. A.; Krauskopf, T.; Minafra, N.; Till, P.; Weiss, M.; Zeier, W. G. Materials Design of Ionic Conductors for Solid State Batteries. *Prog. Energy* **2020**, *2* (2), 022001.

(3)   Culver, S. P.; Koerver, R.; Zeier, W. G.; Janek, J. On the Functionality of Coatings for Cathode Active Materials in Thiophosphate-Based All-Solid-State Batteries. *Adv. Energy Mater.* **2019**, *9* (24), 1900626.

(4)   Morgan, B. J. Lattice-Geometry Effects in Garnet Solid Electrolytes: A Lattice-Gas Monte Carlo Simulation Study. *R. Soc. Open Sci.* **2017**, *4* (11), 170824.

(5)   Krauskopf, T.; Hartmann, H.; Zeier, W. G.; Janek, J. Toward a Fundamental Understanding of the Lithium Metal Anode in Solid-State Batteries - An Electrochemo-Mechanical Study on the Garnet-Type Solid Electrolyte $Li_{6.25}Al_{0.25}La_3Zr_2O_{12}$. *ACS Appl. Mater. Interfaces* **2019**, *11* (15), 14463–14477.

(6)   Sharafi, A.; Kazyak, E.; Davis, A. L.; Yu, S.; Thompson, T.; Siegel, D. J.; Dasgupta, N. P.; Sakamoto, J. Surface Chemistry Mechanism of Ultra-Low Interfacial Resistance in the Solid-State Electrolyte $Li_7La_3Zr_2O_{12}$. *Chem. Mater.* **2017**, *29* (18), 7961–7968.

(7)   Soman, S.; Iwai, Y.; Kawamura, J.; Kulkarni, A. Crystalline Phase Content and Ionic Conductivity Correlation in LATP Glass–Ceramic. *J. Solid State Electrochem. 2011 165* **2011**, *16* (5), 1761–1766.

(8)   Monchak, M.; Hupfer, T.; Senyshyn, A.; Boysen, H.; Chernyshov, D.; Hansen, T.; Schell, K. G.; Bucharsky, E. C.; Hoffmann, M. J.; Ehrenberg, H. Lithium Diffusion Pathway in $Li_{1.3}Al_{0.3}Ti_{1.7}(PO_4)_3$ (LATP) Superionic Conductor. *Inorg. Chem.* **2016**, *55* (6), 2941–2945.

(9)   Bohnke, O. The Fast Lithium-Ion Conducting Oxides $Li_{3x}La_{2/3-x}TiO_3$ from Fundamentals to Application. *Solid State Ionics* **2008**, *179* (1–6), 9–15.

(10)   Kraft, M. A.; Ohno, S.; Zinkevich, T.; Koerver, R.; Culver, S. P.; Fuchs, T.; Senyshyn, A.; Indris, S.;

Morgan, B. J.; Zeier, W. G. Inducing High Ionic Conductivity in the Lithium Superionic Argyrodites $Li_{6+x}P_{1-x}Ge_xS_5I$ for All-Solid-State Batteries. *J. Am. Chem. Soc.* **2018**, *140* (47), 16330–16339.

(11)   Ohno, S.; Helm, B.; Fuchs, T.; Dewald, G.; Kraft, M. A.; Culver, S. P.; Senyshyn, A.; Zeier, W. G. Further Evidence for Energy Landscape Flattening in the Superionic Argyrodites $Li_{6+x}P_{1-x}M_xS_5I$ (M = Si, Ge, Sn). *Chem. Mater.* **2019**, *31* (13), 4936–4944.

(12)   Kraft, M. A.; Culver, S. P.; Calderon, M.; Böcher, F.; Krauskopf, T.; Senyshyn, A.; Dietrich, C.; Zevalkink, A.; Janek, J.; Zeier, W. G. Influence of Lattice Polarizability on the Ionic Conductivity in the Lithium Superionic Argyrodites Li_6PS_5X (X = Cl, Br, I). *J. Am. Chem. Soc.* **2017**, *139* (31), 10909–10918.

(13)   Zhou, L.; Minafra, N.; Zeier, W. G.; Nazar, L. F. Innovative Approaches to Li-Argyrodite Solid Electrolytes for All-Solid-State Lithium Batteries. *Acc. Chem. Res.* **2021**, *54* (12), 2717–2728.

(14)   Minafra, N.; Culver, S. P.; Li, C.; Senyshyn, A.; Zeier, W. G. Influence of the Lithium Substructure on the Diffusion Pathways and Transport Properties of the Thio-LISICON $Li_4Ge_{1-x}Sn_xS_4$. *Chem. Mater.* **2019**, *31* (10), 3794–3802.

(15)   Minafra, N.; Hogrefe, K.; Barbon, F.; Helm, B.; Li, C.; Wilkening, H. M. R.; Zeier, W. G. Two-Dimensional Substitution: Toward a Better Understanding of the Structure–Transport Correlations in the Li-Superionic Thio-LISICONs. *Chem. Mater.* **2021**, *33* (2), 727–740.

(16)   Kanno, R.; Murayama, M. Lithium Ionic Conductor Thio-LISICON: The Li_2S-GeS_2-P_2S_5 System. *J. Electrochem. Soc.* **2001**, *148* (7), A742.

(17)   Kamaya, N.; Homma, K.; Yamakawa, Y.; Hirayama, M.; Kanno, R.; Yonemura, M.; Kamiyama, T.; Kato, Y.; Hama, S.; Kawamoto, K.; et al. A Lithium Superionic Conductor. *Nat. Mater.* **2011**, *10* (9), 682–686.

(18)   Krauskopf, T.; Culver, S. P.; Zeier, W. G. Bottleneck of Diffusion and Inductive Effects in $Li_{10}Ge_{1-x}Sn_xP_2S_{12}$. *Chem. Mater.* **2018**, *30* (5), 1791–1798.

(19)   Weber, D. A.; Senyshyn, A.; Weldert, K. S.; Wenzel, S.; Zhang, W.; Kaiser, R.; Berendts, S.; Janek, J.; Zeier, W. G. Structural Insights and 3D Diffusion Pathways within the Lithium Superionic Conductor $Li_{10}GeP_2S_{12}$. *Chem. Mater.* **2016**, *28* (16), 5905–5915.

(20)   Kato, Y.; Hori, S.; Kanno, R. $Li_{10}GeP_2S_{12}$-Type Superionic Conductors: Synthesis, Structure, and Ionic Transportation. *Adv. Energy Mater.* **2020**, *10* (42), 2002153.

(21)   Muy, S.; Bachman, J. C.; Giordano, L.; Chang, H. H.; Abernathy, D. L.; Bansal, D.; Delaire, O.; Hori, S.; Kanno, R.; Maglia, F.; et al. Tuning Mobility and Stability of Lithium Ion Conductors Based on Lattice Dynamics. *Energy Environ. Sci.* **2018**, *11* (4), 850–859.

(22)   Han, F.; Zhu, Y.; He, X.; Mo, Y.; Wang, C. Electrochemical Stability of $Li_{10}GeP_2S_{12}$ and $Li_7La_3Zr_2O_{12}$ Solid Electrolytes. *Adv. Energy Mater.* **2016**, *6* (8), 1–9.

(23)   Schlem, R.; Banik, A.; Ohno, S.; Suard, E.; Zeier, W. G. Insights into the Lithium Sub-Structure of Superionic Conductors Li_3YCl_6 and Li_3YBr_6. *Chem. Mater.* **2021**, *33* (1), 327–337.

(24)   Asano, T.; Sakai, A.; Ouchi, S.; Sakaida, M.; Miyazaki, A.; Hasegawa, S. Solid Halide Electrolytes with High Lithium-Ion Conductivity for Application in 4 V Class Bulk-Type All-Solid-State Batteries. *Adv. Mater.* **2018**, *30* (44), 1803075.

(25)   Duchêne, L.; Remhof, A.; Hagemann, H.; Battaglia, C. Status and Prospects of Hydroborate Electrolytes for All-Solid-State Batteries. *Energy Storage Mater.* **2019**.

(26)   Li, X.; Liang, J.; Yang, X.; Adair, K. R.; Wang, C.; Zhao, F.; Sun, X. Progress and Perspectives on Halide Lithium Conductors for All-Solid-State Lithium Batteries. *Energy Environ. Sci.* **2020**, *13* (5), 1429–1461.

(27)   Hayashi, A.; Masuzawa, N.; Yubuchi, S.; Tsuji, F.; Hotehama, C.; Sakuda, A.; Tatsumisago, M. A Sodium-Ion Sulfide Solid Electrolyte with Unprecedented Conductivity at Room Temperature. *Nat. Commun. 2019 101* **2019**, *10* (1), 1–6.

(28)   Kraft, M. A.; Gronych, L. M.; Famprikis, T.; Ohno, S.; Zeier, W. G. Structure and Sodium Ion Transport in $Na_{11+x}Sn_{2+x}(Sb_{1-y}P_y)_{1-x}S_{12}$. *Chem. Mater.* **2020**, *32* (15), 6566–6576.

(29)   Schlem, R.; Banik, A.; Eckardt, M.; Zobel, M.; Zeier, W. G. $Na_{3-x}Er_{1-x}Zr_xCl_6$—A Halide-Based Fast Sodium-Ion Conductor with Vacancy-Driven Ionic Transport. *ACS Appl. Energy Mater.* **2020**, *3* (10), 10164–10173.

(30)   Fuchs, T.; Culver, S. P.; Till, P.; Zeier, W. G. Defect-Mediated Conductivity Enhancements in $Na_{3-x}Pn_{1-x}W_xS_4$ (Pn = P, Sb) Using Aliovalent Substitutions. *ACS Energy Lett.* **2020**, *5* (1), 146–151.

(31)   Hwang, J.-Y.; Myung, S.-T.; Sun, Y.-K. Sodium-Ion Batteries: Present and Future. *Chem. Soc. Rev.* **2017**, *46* (12), 3529–3614.

(32)   Yabuuchi, N.; Kubota, K.; Dahbi, M.; Komaba, S. Research Development on Sodium-Ion Batteries. *Chem. Rev.* **2014**, *114* (23), 11636–11682.

(33)   Hayashi, A.; Masuzawa, N.; Yubuchi, S.; Tsuji, F.; Hotehama, C.; Sakuda, A.; Tatsumisago, M. A Sodium-Ion Sulfide Solid Electrolyte with Unprecedented Conductivity at Room Temperature. *Nat. Commun.* **2019**, *10*.

(34)   Krauskopf, T.; Culver, S. P.; Zeier, W. G. Local Tetragonal Structure of the Cubic Superionic Conductor Na_3PS_4. *Inorg. Chem.* **2018**, *57* (8), 4739–4744.

(35)   Zhang, D.; Cao, X.; Xu, D.; Wang, N.; Yu, C.; Hu, W.; Yan, X.; Mi, J.; Wen, B.; Wang, L.; et al. Synthesis of Cubic Na_3SbS_4 Solid Electrolyte with Enhanced Ion Transport for All-Solid-State Sodium-Ion Batteries. *Electrochim. Acta* **2018**, *259*, 100–109.

(36)   Tsuji, F.; Masuzawa, N.; Sakuda, A.; Tatsumisago, M.; Hayashi, A. Preparation and Characterization of Cation-Substituted Na_3SbS_4 Solid Electrolytes. *ACS Appl. Energy Mater.* **2020**, *3* (12), 11706–11712.

(37)   Gamo, H.; Phuc, N. H. H.; Muto, H.; Matsuda, A. Effects of Substituting S with Cl on the Structural and Electrochemical Characteristics of Na_3SbS_4 Solid Electrolytes. *ACS Appl. ENERGY Mater.* **2021**, *4* (6), 6125–6134.

(38)   Jalem, R.; Hayashi, A.; Tsuji, F.; Sakuda, A.; Tateyama, Y. First-Principles Calculation Study of Na+ Superionic Conduction Mechanism in W- and Mo-Doped Na_3SbS_4 Solid Electrolytes. *Chem. Mater.* **2020**, *32* (19), 8373–8381.

(39)   Banik, A.; Famprikis, T.; Ghidiu, M.; Ohno, S.; Kraft, M. A.; Zeier, W. G. On the Underestimated Influence of Synthetic Conditions in Solid Ionic Conductors. *Chem. Sci.* **2021**, *12* (18), 6238–6263.

(40)   Wu, E. A.; Kompella, C. S.; Zhu, Z. Y.; Lee, J. Z.; Lee, S. C.; Chu, I. H.; Nguyen, H.; Ong, S. P.; Banerjee, A.; Meng, Y. S. New Insights into the Interphase between the Na Metal Anode and Sulfide Solid-State Electrolytes: A Joint Experimental and Computational Study. *ACS Appl. Mater. Interfaces* **2018**, *10* (12), 10076–10086.

(41)   Park, K. H.; Kim, D. H.; Kwak, H.; Jung, S. H.; Lee, H.-J.; Banerjee, A.; Lee, J. H.; Jung, Y. S. Solution-

22

Derived Glass-Ceramic NaI·Na$_3$SbS$_4$ Superionic Conductors for All-Solid-State Na-Ion Batteries. *J. Mater. Chem. A* **2018**, *6* (35), 17192–17200.

(42)   Ohno, S.; Bernges, T.; Buchheim, J.; Duchardt, M.; Hatz, A. K.; Kraft, M. A.; Kwak, H.; Santhosha, A. L.; Liu, Z.; Minafra, N.; et al. How Certain Are the Reported Ionic Conductivities of Thiophosphate-Based Solid Electrolytes? An Interlaboratory Study. *ACS Energy Lett.* **2020**, *5* (3), 910–915.

(43)   Cronau, M.; Szabo, M.; König, C.; Wassermann, T. B.; Roling, B. How to Measure a Reliable Ionic Conductivity? The Stack Pressure Dilemma of Microcrystalline Sulfide-Based Solid Electrolytes. *ACS Energy Lett.* **2021**, *6* (9), 3072–3077.

(44)   Hayashi, A.; Tsuji, F.; Masuzawa, N.; Sakuda, A.; Tatsumisago, M. Cation-Substituted Na$_3$SbS$_4$ Electrolyte with High Sodium-Ion Conductivity. *ECS Meet. Abstr.* **2020**, *MA2020-02* (5), 969.

(45)   Coelho, A. A. TOPAS-Academic. *Coelho Software, Brisbane, Aust.* **2007**.

(46)   Momma, K.; Izumi, F.; IUCr. VESTA 3 for Three-Dimensional Visualization of Crystal, Volumetric and Morphology Data. *urn:issn:0021-8898* **2011**, *44* (6), 1272–1276.

(47)   Lany, S.; Zunger, A. Accurate Prediction of Defect Properties in Density Functional Supercell Calculations. *Model. Simul. Mater. Sci. Eng.* **2009**, *17* (8), 084002.

(48)   Perdew, J. P.; Burke, K.; Ernzerhof, M. Generalized Gradient Approximation Made Simple. *Phys. Rev. Lett.* **1996**, *77* (18), 3865–3868.

(49)   Kresse, G.; Furthmüller, J. Efficiency of Ab-Initio Total Energy Calculations for Metals and Semiconductors Using a Plane-Wave Basis Set. *Comput. Mater. Sci.* **1996**, *6* (1), 15–50.

(50)   Gorai, P.; Long, H.; Jones, E.; Santhanagopalan, S.; Stevanović, V. Defect Chemistry of Disordered Solid-State Electrolyte Li$_{10}$GeP$_2$S$_{12}$. *J. Mater. Chem. A* **2020**, *8* (7), 3851–3858.

(51)   Peng, H.; Scanlon, D. O.; Stevanovic, V.; Vidal, J.; Watson, G. W.; Lany, S. Convergence of Density and Hybrid Functional Defect Calculations for Compound Semiconductors. *Phys. Rev. B - Condens. Matter Mater. Phys.* **2013**, *88* (11), 115201.

(52)   Goyal, A.; Gorai, P.; Peng, H.; Lany, S.; Stevanović, V. A Computational Framework for Automation of Point Defect Calculations. *Comput. Mater. Sci.* **2017**, *130*, 1–9.

(53)   Ohno, S.; Imasato, K.; Anand, S.; Tamaki, H.; Kang, S. D.; Gorai, P.; Sato, H. K.; Toberer, E. S.; Kanno, T.; Snyder, G. J. Phase Boundary Mapping to Obtain N-Type Mg$_3$Sb$_2$-Based Thermoelectrics. *Joule* **2018**, *2* (1), 141–154.

(54)   Brug, G. J.; van den Eeden, A. L. G.; Sluyters-Rehbach, M.; Sluyters, J. H. The Analysis of Electrode Impedances Complicated by the Presence of a Constant Phase Element. *J. Electroanal. Chem.* **1984**, *176* (1–2), 275–295.

(55)   Irvine, J. T. S.; Sinclair, D. C.; West, A. R. Electroceramics: Characterization by Impedance Spectroscopy. *Adv. Mater.* **1990**, *2* (3), 132–138.

(56)   Ohno, S.; Aydemir, U.; Amsler, M.; Pöhls, J. H.; Chanakian, S.; Zevalkink, A.; White, M. A.; Bux, S. K.; Wolverton, C.; Snyder, G. J. Achieving ZT > 1 in Inexpensive Zintl Phase Ca$_9$Zn$_{4+x}$Sb$_9$ by Phase Boundary Mapping. *Adv. Funct. Mater.* **2017**, *27* (20), 1606361.

(57)   Wood, M.; Toriyama, M. Y.; Dugar, S.; Male, J.; Anand, S.; Stevanović, V.; Snyder, G. J. Phase Boundary Mapping of Tin-Doped ZnSb Reveals Thermodynamic Route to High Thermoelectric Efficiency. *Adv.*

Energy Mater. **2021**, *11* (20), 2100181.

(58)   Crawford, C. M.; Ortiz, B. R.; Gorai, P.; Stevanovic, V.; Toberer, E. S. Experimental and Computational Phase Boundary Mapping of Co₄Sn₆Te₆. *J. Mater. Chem. A* **2018**, *6* (47), 24175–24185.

(59)   Li, X.; Yang, P.; Wang, Y.; Zhang, Z.; Qin, D.; Xue, W.; Chen, C.; Huang, Y.; Xie, X.; Wang, X.; et al. Phase Boundary Mapping in ZrNiSn Half-Heusler for Enhanced Thermoelectric Performance. *Research* **2020**, *2020*, 1–9.

(60)   Jood, P.; Male, J. P.; Anand, S.; Matsushita, Y.; Takagiwa, Y.; Kanatzidis, M. G.; Snyder, G. J.; Ohta, M. Na Doping in PbTe: Solubility, Band Convergence, Phase Boundary Mapping, and Thermoelectric Properties. *J. Am. Chem. Soc.* **2020**, *142* (36), 15464–15475.

(61)   Male, J.; Agne, M. T.; Goyal, A.; Anand, S.; Witting, I. T.; Stevanović, V.; Snyder, G. J. The Importance of Phase Equilibrium for Doping Efficiency: Iodine Doped PbTe. *Mater. Horizons* **2019**, *6* (7), 1444–1453.